Materials Science in Semiconductor Processing 153 (2023) 107191

Contents lists available at ScienceDirect

Materials Science in Semiconductor Processing

journal homepage: www.elsevier.com/locate/mssp

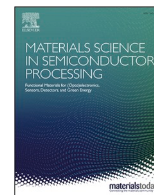

High-quality single-crystalline epitaxial regrowth on pulsed laser melting of Ti implanted GaAs

S. Algaidy [a,*], D. Caudevilla [a], F. Perez-Zenteno [a], R. García-Hernansanz [a], E. García-Hemme [a], J. Olea [a], E. San Andrés [a], S. Duarte-Cano [a], J. Siegel [b], J. Gonzalo [b], D. Pastor [a,**], A. del Prado [a,***]

[a] Dpt. Estructura de la Materia, Física Térmica y Electrónica, Fac. CC.Física, Univ. Complutense de Madrid, 28040, Spain
[b] Laser Processing Group, Instituto de Óptica, IO-CSIC, Serrano 121, 28006, Madrid, Spain

ARTICLE INFO

Keywords:
Gallium compounds
Ion implantation
Pulsed laser melting
Supersaturated material
Titanium

ABSTRACT

We present a detailed investigation on the formation of supersaturated GaAs using Ti^{+} implantation followed by nanosecond Pulsed Laser Melting (PLM). We have synthesized high-crystal quality supersaturated GaAs layers with concentrations of Ti above the insulator to metal transition (Mott limit). The Ti-implanted concentration depth profiles after PLM obtained by Time-of-Flight Secondary Ion Mass Spectroscopy (ToF-SIMS) show a redistribution of Ti impurities within the first hundred nanometers and superficial concentration up to 1×10^{21} cm^{-3}. Raman spectroscopy of these Ti supersaturated, and regrown GaAs samples shows a sharp crystalline peak and tensile strain due to the Ti lattice incorporation. Scanning Transmission Electron Microscopy (STEM) and high-resolution Transmission Electron Microscopy (TEM) images show a good GaAs crystallinity after the PLM process. Energy-Dispersive X-ray Spectroscopy (EDS) reveals an enhanced Ti signal inside bubble-like structures and an appearance of interface oxide layer with all processed samples.

1. Introduction

The evolution of semiconductor materials plays an important role in improving current technologies. Many efforts have been devoted to increase the capabilities of semiconductors for different applications. In the photovoltaics field, intermediate band materials were proposed in 1997 [1] as a kind of semiconductor material which can absorb photons at energies below the bandgap, and therefore could improve the efficiency of solar cells or extend the detection range of photodetectors [2,3]. Multiple approaches have been suggested to obtain intermediate band materials, such as: highly mismatched alloys or dilute semiconductor alloys [4,5], quantum dots [6] and hyperdoping beyond the insulator to metal transition (Mott limit) [7].

Hyperdoping with deep level impurities has been proved to produce infrared photoresponse at room temperature for different systems based on Si. It was achieved by ion implantation followed by pulsed laser melting (PLM): Si:S [8], Si:Au [9], Si:Ti [10], Si:V [11], Si:Te [12] or flash lamp annealing Si:Se [13]. Solar cell prototypes based on Si hyperdoped with Ti have exhibited sub-bandgap quantum efficiency which would agree with the intermediate band formation [14]. Infrared photodetectors based on hyperdoped Germanium with chalcogenides (Se, Te) or Au show sub-bandgap Near-IR photodetection at room temperature [15]. Hyperdoped III-V semiconductors have shown sub-bandgap photoresponse for Ti hyperdoped GaP at room temperature [16–18]. Furthermore, sub-bandgap absorption has been achieved by means of electronic band engineering in high mismatched alloys of GaNAs [19]. However, all these hyperdoped semiconductors are based on indirect bandgap semiconductors. Direct bandgap materials would be desired to improve the optoelectronic photoresponse.

GaAs is one of the most used compound semiconductors for photodetectors and photovoltaic applications due to its capacity of direct bandgap photon absorption [20]. In fact, hyperdoped GaAs with deep level centres has been proposed as a good candidate to produce an intermediate band material [2,3]. The capability to absorb sub-bandgap photons would potentially enable the fabrication of near-infrared GaAs based photodetectors and solar cells [21]. The uses of GaAs in

* Corresponding author.
*** Corresponding author.
** Corresponding author.
E-mail addresses: Sarialga@ucm.es (S. Algaidy), dpastor@ucm.es (D. Pastor), adelprado@ucm.es (A. del Prado).

https://doi.org/10.1016/j.mssp.2022.107191
Received 29 June 2022; Received in revised form 7 October 2022; Accepted 25 October 2022
Available online 31 October 2022
1369-8001/© 2022 The Authors. Published by Elsevier Ltd. This is an open access article under the CC BY-NC-ND license (http://creativecommons.org/licenses/by-nc-nd/4.0/).

current technology reach many specialized sectors that range from nano-scale manipulation, such as, quantum dots and nanowires [22,23], to graphene-based technology [24,25], and thin films technology [26]. Many of these developing technologies uses GaAs substrates due to its well-known and exceptional properties [22–26]. Beside optoelectronic applications, hyperdoping GaAs with suitable impurities, such as Mn and Fe, can produce ferromagnetic properties that can be implemented in spintronic technologies [27–29].

Based on the results obtained on hyperdoping Si, Ge, and GaP [10,15,16], in this work we study the approach of hyperdoping GaAs with Ti by ion implantation followed by pulsed laser melting (PLM). The goal is to obtain high-quality single-crystalline epitaxially regrown layers, which is one of the main challenges faced by this technology [30–33].

Previous results on III-V semiconductors (GaP) showed a specific PLM fluence window for which the implanted samples completely recovered the crystallinity, which was proved by mobility measurements after the PLM process [17]. To determine the optimum processing parameters for implanted GaAs, we have fabricated samples with a specific range of laser melting fluences (0.30–0.65 J/cm^2) with a 0.05 J/cm^2 step for a single implantation dose (2×10^{15} cm^{-2}). Structural characterization of the implanted and PLM processed samples has been performed by means of ToF-SIMS, Raman spectroscopy, TEM, STEM and EDS to analyse the impurity concentration, depth profile, crystallinity, and composition, respectively.

In this work, we demonstrate that the combination of ion implantation followed by PLM is a suitable technique to obtain high quality crystalline Ti-supersaturated GaAs with concentrations above the Mott limit in a thickness up to approximately 50 nm. Furthermore, an oxide surface layer appears with all the samples after the PLM process. Bubble-like features are also observed on the implanted and PLM samples that exhibit a high Ti concentration.

2. Experimental

Single side polished, undoped semi-insulating <100> GaAs wafers, 350 μm thick with a resistivity of 5.5×10^8 Ω cm at room temperature and a mobility of 5000 cm^2/V s were implanted on the polished surface in a refurbished VARIAN CF3000 ion implanter with a $^{48}Ti^+$ dose of 2×10^{15} cm^{-2} at an energy of 32 keV. The implantation was conducted using a 7° tilt angle, to reduce channelling [34]. The implanted wafers were cut in 5 × 5 mm^2 samples for processing with the different PLM conditions.

After ion implantation, the crystal lattice is damaged and thermal processes are required to restore the crystallinity. The implanted samples were irradiated with an ArF^+ excimer pulsed laser in ambient air (λ = 193 nm, with a pulse duration of 20 ns full width half maximum). The laser beam was homogenized in a square spot area of 1 × 1 mm^2 on the sample surface. The 5 × 5 mm^2 sample area was processed by overlapping single pulses across the irradiation plane. The overlapping between consecutive horizontal and vertical irradiated areas was 5 and 10 μm, respectively. To analyse separately the PLM effect in the GaAs samples, also a set of unimplanted GaAs samples was prepared, and PLM processed in the same conditions as the implanted ones.

The depth concentration profile of Ti on the GaAs samples was obtained by ToF-SIMS measurements using an ION-TOF-SIMS model IV. The area of interest selected for the SIMS measurements was inside a single irradiation pulse. This way we avoided the overlapping area, which receives more than one pulse, and therefore maximise the accuracy of the desired SIMS profile. The sputtering beam creates a 450 × 450 μm^2 spot size. However, the analysed area was slightly smaller (250 × 250 μm^2), to avoid crater edge effects. The primary pulsed ion beam consisted of Bi^{3+} with incident energy of 25 keV and an O_2^+ sputtering gun was used with an energy of 1 keV. Both ion beam and sputtering gun were tilted at a 45° angle. As-implanted samples were also analysed using ToF-SIMS for calibration purposes. The crater depth was characterized by optical profilometry using white light interferometry and a constant erosion rate was assumed for the sputtering gun. The ToF-SIMS was conducted under high-vacuum environment of 3.3×10^{-8} mbar.

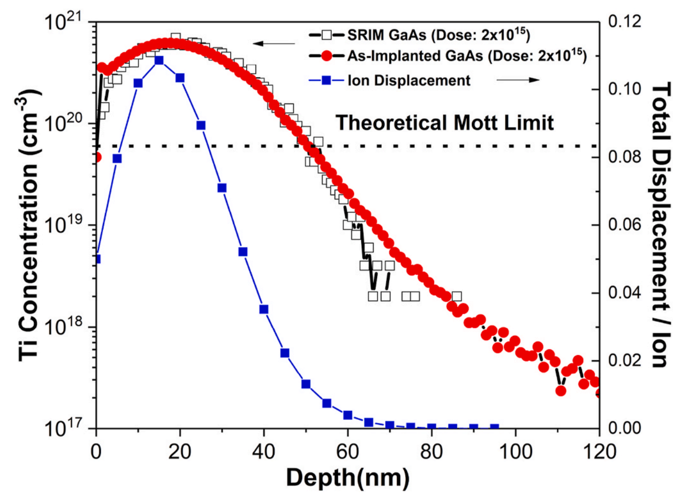

Fig. 1. (Left) As implanted and SRIM simulation of Ti Implanted GaAs with 2×10^{15} cm^{-2}. (Right) total displacements per ion produced by SRIM software.

The Raman scattering spectra were analysed using an Olympus BXFM microscope equipped with a coupled charge detector model AndoriDus DU-420 Peltier cooled. The scattered light was recorded at room temperature in unpolarized backscattering configuration using a 532 nm laser with a power of 22 mW. Three points were chosen randomly across the surface of the samples for averaging.

To analyse the crystal quality and elemental composition of the implanted samples, cross -section TEM, STEM and EDS was used. Lamellae from a reference substrate, an as-implanted reference, an implanted and PLM processed samples at different energies were extracted using Focused Ion Beam Scanning Electron Microscopy (FIB-SEM), with a Helios Nanolab 650 model. To protect the area of interest a layer of 200 nm of C rich Pt was deposited by focused electron beam induced deposition (FIBID) at 5 kV and 1.6 nA. Subsequently, a layer of about 1.2 μm of Pt was deposited by FIBID on the same area. FIBID worked at 30 kV and 0.23 nA. For the milling of trenches, polishing and undercutting of the lamellas, FIB at 30 kV was used with 2.5 nA, 0.23 nA and 2.5 nA, respectively. An Omniprobe nanomanipulator was used to weld the lamellas with Pt and move it to a copper holder. After that, a final thinning was performed by FIB at 5 kV and 0.68 nA to obtain a lamella of about 5–7 μm × 50 nm. The structure was analysed by obtaining TEM images in a JEOL JEM 3000F microscope operating at 300 keV, which is also the excitation energy for the EDS measurements. The scanning mode with a JEOL annular dark field detector with a beam diameter of about 0.7 nm was used.

3. Results and discussion

The impurity profile distribution can be simulated using Montecarlo method with the Stopping and Range of Ions in Matter (SRIM) package [35]. These simulations predict the ion depth distribution of the implanted impurities in an amorphous host semiconductor. Typically, the ion implantations in crystalline host semiconductors are performed with a 7° tilt angle, as it has been done in this work, to minimize channelling effects and to produce random collisions of the ions with the lattice atoms, as it is the case with an amorphous layer. Fig. 1 shows the Ti-concentration depth-profile of the as-implanted GaAs substrate obtained by ToF-SIMS, along with the results of the SRIM simulations. The figure also shows the total displacement of ions simulated by the SRIM software. The total areas of the ToF-SIMS measurement and SRIM simulation, have been normalized to the implanted dose. The ToF-SIMS experimental results show the expected gaussian depth-profile

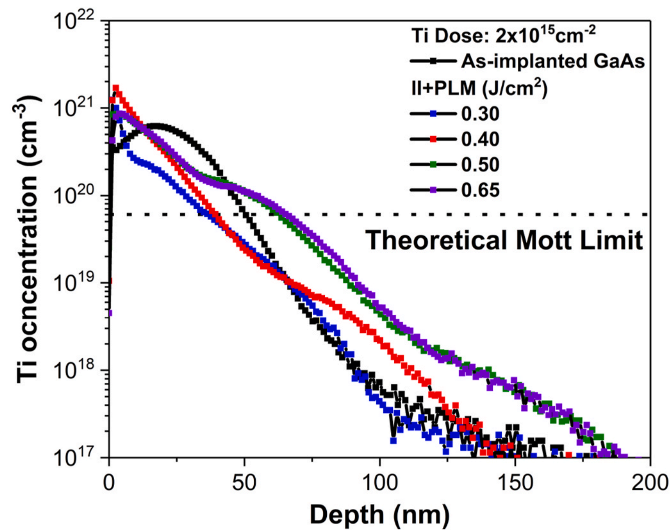

Fig. 2. ToF-SIMS of GaAs:Ti for the as-implanted and samples subjected to PLM at different laser fluences.

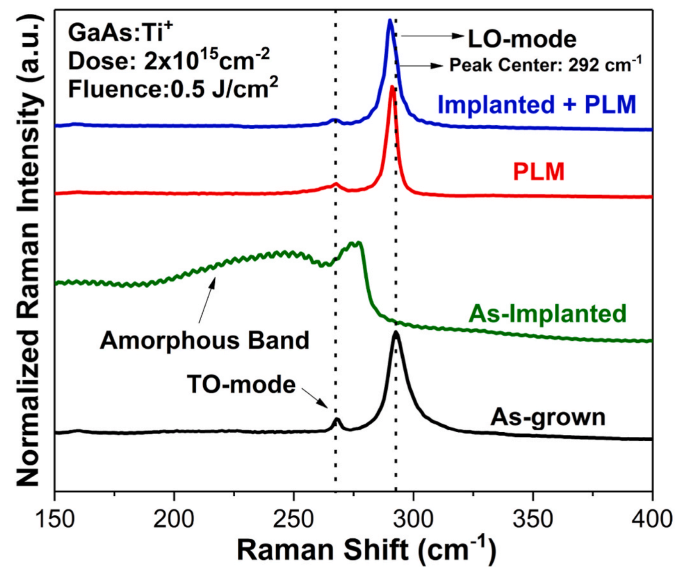

Fig. 3. Raman Spectroscopy of as-implanted, reference, implanted and laser melted GaAs.

distribution of Ti, which is in good agreement with the SRIM simulations, yet some differences are observed in the ToF-SIMS gaussian tail curve due to the residual channel effect. The experimental curve presents a Ti concentration above the theoretical insulator to metal transition for a thickness of 50 nm.

Fig. 2 shows the ToF-SIMS profiles of the four samples processed at different PLM fluences (0.30, 0.40, 0.50 and 0.65 J/cm^2) and the as-implanted GaAs sample. The fluence range has been selected based on the previous observation of a laser process window in GaAs [36], for which the highest crystal quality and the lowest electrical resistivities are obtained. This process window depends on the amorphous layer thickness, the laser wavelength, and the laser fluence [30]. We have selected an initial fluence that exceeds the superficial melt threshold of the a-GaAs and the c-GaAs.

For the PLM processed samples, the ToF-SIMS concentration has been estimated assuming the same relationship between counts and actual concentration than in the as-implanted sample. Yet, it must be noted that the ionization rate depends also on structural factors, such as the crystallinity. Since the as-implanted sample is amorphous and the PLM processed samples recover the crystallinity, these concentrations can only be considered as estimations. For the PLM energies of 0.40 J/cm^2 and higher, following this procedure would lead to a total Ti integrated area higher than the actual implanted dose, which is not possible. As a better approach, the total area has been normalized to the implanted dose. Furthermore, to better understand the relation between the laser fluence and surface temperature during the irradiation time, a simulation of the laser melting process has been conducted. (Check Fig. 1.1 of supplementary document).

After the PLM process there is a clear redistribution of the impurities, with an accumulation of Ti close to the surface and for the highest PLM fluence used, Ti extends beyond the as-implanted profile. This behaviour can be explained considering the dynamics of the PLM process. In a first step, a layer of the film is melted and in this liquid phase the impurities redistribute in all directions, in particularly, deeper towards the melt/solid interface. In a second stage, the melted region rapidly recrystallizes starting from the crystalline seed of the substrate underneath the implanted layer. The impurities are pushed towards the surface of the film, accumulating the maximum concentration very close to the surface [37]. During this process, instabilities in the solidifying front can occur leading to the accumulation of Ti in the characteristic structures known as cellular breakdown [38]. When this happens, ToF-SIMS results usually show mesa like features. These features are not observed in our samples, suggesting that no cellular breakdown is taking place [38]. This was also confirmed by the cross-section TEM and STEM images discussed below.

In a previously published paper [30], it was explained that the melting of the GaAs surface occurs after a threshold fluence is overpassed. This threshold fluence is estimated around 0.08 J/cm^2 for amorphous GaAs and 0.2 J/cm^2 for crystalline GaAs [39]. Further examination of the samples shows another threshold for the melting and solidification of the entire implanted-amorphous layer which is produced from the undamaged crystalline seed of the substrate. In other words, below this threshold the laser fluence is not sufficient to fully melt the amorphous layer, although polycrystalline re-solidification still occurs. This phenomenon, known as explosive crystallization, is produced because the latent heat during the crystallization of a thin molten layer is sufficient to induce melting of a thin amorphous layer underneath. Which crystallizes upon solidification and leads to a melting of the underlying amorphous layer, and so on. As a result, an inward propagating melt front is produced even for initial shallow melt depth, leaving behind polycrystalline material. In other words, the latent heat of the liquid-crystalline transition is higher than that of the liquid-amorphous transition, with the thermal diffusivity of the amorphous phase being relatively low [30,37,40].

By analyzing the shape of the redistributed Ti profiles in Fig. 2, it seems that the PLM process has been able to melt the whole implanted layer even for the lowest laser fluence used. It can also be concluded from the ToF-SIMS results that a high concentration of Ti, well above the insulator to metal transition is achieved in a thickness around 35–65 nm (depending on the PLM energy fluence used), demonstrating that the combination of ion implantation and PLM is a suitable technique for supersaturating GaAs. It is also worth mentioning that there were no detectable losses of Ga and As during the PLM and Ion implantation process. (Check Fig. 2.1 of supplementary document).

Fig. 3 shows the normalized Raman spectra of four representative samples (substrate reference, as implanted, just processed by PLM, and implanted and processed by PLM at 0.50 J/cm^2). The reference sample shows the crystalline peak corresponding to the LO-mode located at 292 cm^{-1} [41–43]. The TO-mode is symmetry-forbidden in the (100) plane of a perfect crystalline GaAs. However, it can be observed as a low intensity peak in all the samples of the figure. This is due to the sample contribution out of plane in the backscattering configuration [42]. The probing depth of the Raman laser excitation wavelength of 532 nm for GaAs is approximately 60 nm, which ensures probing of the just

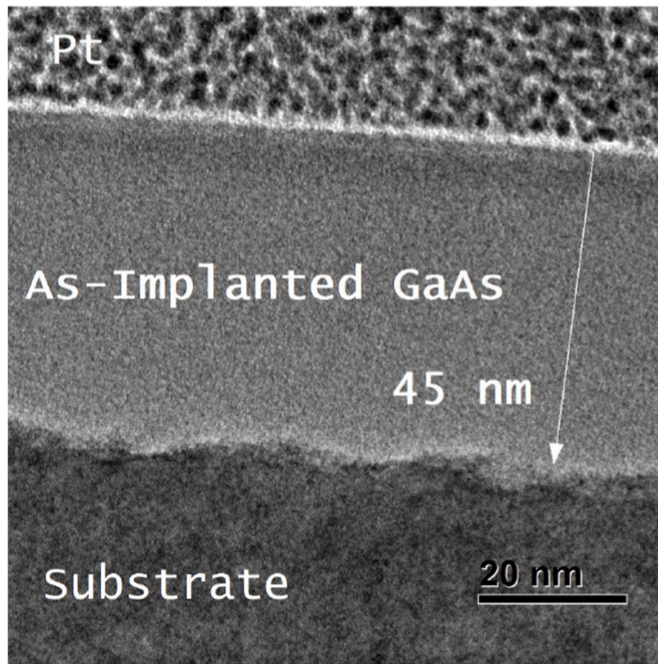

Fig. 4. Cross-section TEM image of As-implanted GaAs.

implanted layer. After implantation, the characteristic broadband related to the amorphous GaAs is observed around 250 cm^{-1} [43]. A broadband LO-mode together with a redshift can be detected at 275 cm^{-1} in agreement with previous reports [43]. This amorphous band is consistent with the high implantation dose used (2×10^{15} cm^{-2}) [42, 43]. Implantation with doses up to 5×10^{12} cm^{-2} should not cause a significant broadening of the LO-mode [41]. For the just PLM processed sample, a slight red shift of the LO-mode from 292 cm^{-1} to 290 cm^{-1} is observed. This shift is induced by lattice strains attributed to the laser melting process [41–45]. It can also be observed a narrowing of the LO-mode, which is characteristic of the phonon scattering in a defect-free crystalline GaAs [40].

The behavior of the implanted and PLM processed sample are essentially the same as the not implanted PLM sample, indicating that the PLM process can recover the crystalline quality of the implanted layer. When varying the PLM fluence for the samples, the results do not vary significantly, neither for the only PLM processed samples nor the implanted and PLM processed samples. The samples do not present polycrystallinity since the relation between the LO and TO modes does not change. If that was the case, an increase of the TO mode peak intensity would occur due to the contributions out of plane of the backscattering configuration related to different crystal orientations [17]. This indicates that the fluences used is sufficient to melt the entire amorphous layer, resolidifying from the underneath crystalline layer. In conclusion, the Raman results indicate a high crystalline quality after PLM and strain presence related to the Ti lattice incorporation and PLM processing. We do not detect differences in the Raman spectra between different PLM fluences used.

TEM analysis of the reference sample does not show any visible defects, as expected (Check Fig. 3.1 of supplementary document). Fig. 4 shows a cross-section image of as-implanted GaAs with Ti. After the implantation process, an amorphous layer appears on the first 45 nm of the sample. According to the SRIM simulation and SIMS measurements shown in Fig. 1, the Ti concentration corresponding to this thickness is about 2×10^{20} cm^{-3}. For concentrations below this value, the amorphous layer is not observed. This also can be observed by the ion displacements produced by the implantation which correspond approximately to 45 nm.

Fig. 5 shows the TEM images of representative implanted and non-implanted samples, processed at different PLM fluences. The images do not exhibit visible extended defects on the processed region. The

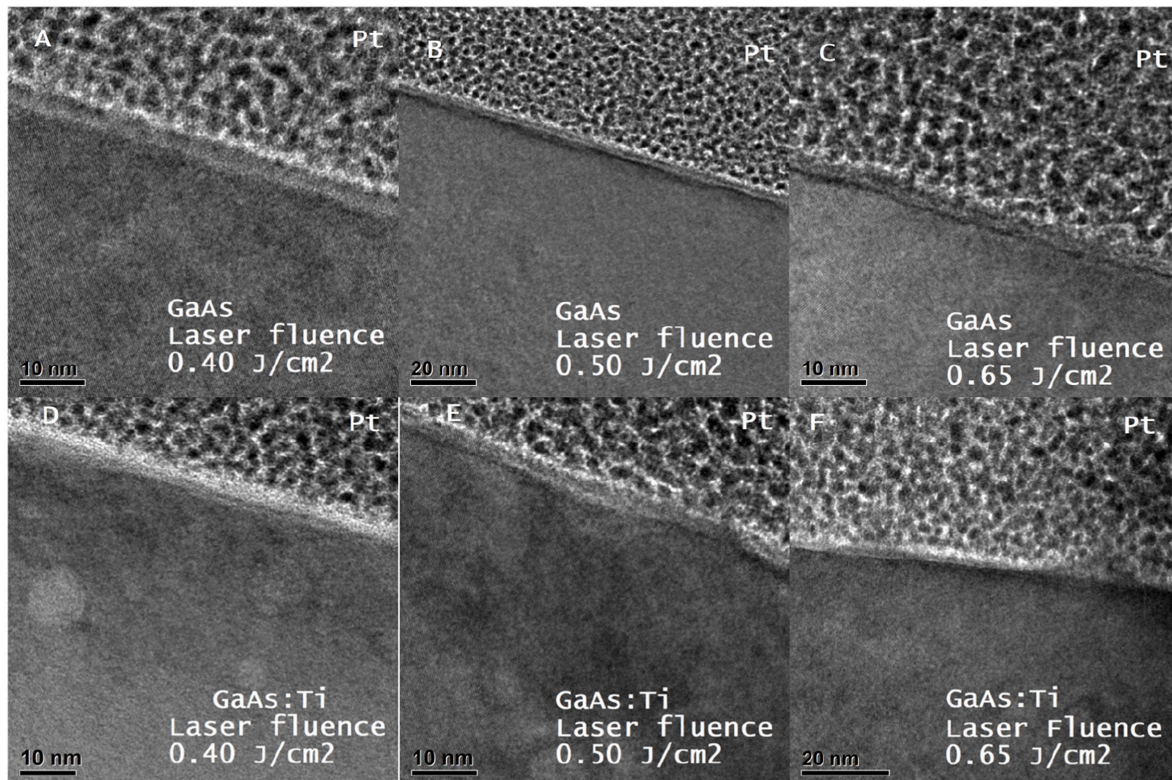

Fig. 5. TEM images of non-implanted and implanted GaAs at different PLM laser fluences.

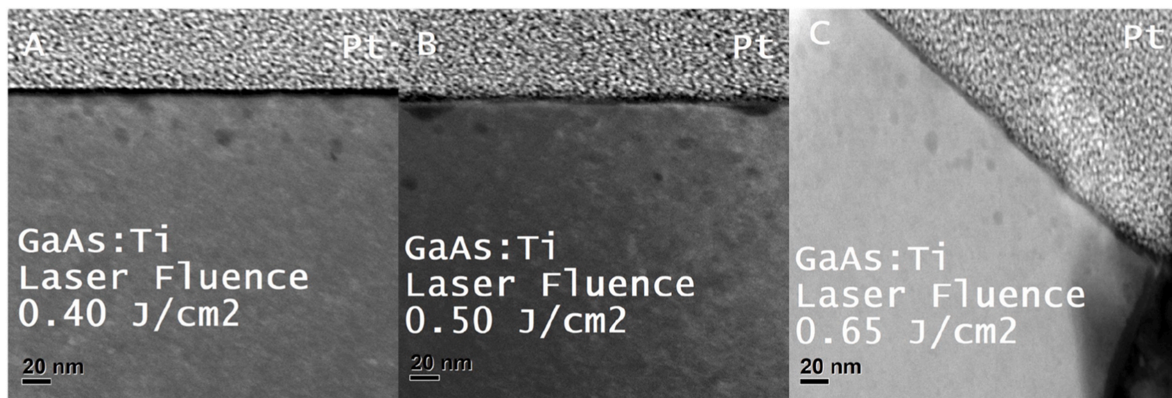

Fig. 6. STEM images of implanted GaAs at different PLM laser fluences.

Fig. 7. EDS signal of GaAs:Ti processed by PLM at 0.50 J/cm^2 laser fluence. Top: Measurement path. Middle: Ti signal. Bottom: O signal.

absence of polycrystallinity agrees with Raman measurements, indicating the re-solidification originated in the underneath crystalline layer. Annealing processes can create vacancies in the material as well as extended defects such as stacking faults, grain boundaries, etc [5]. No such extended defects can be observed in our samples. Besides, no features characteristic of cellular breakdown taking place during the solidification are observed either. However, in the case of the implanted sample, bubble-like structures are observed for the PLM fluences analysed (0.4, 0.5 and 0.65 J/cm^2). These bubble-like structures have also been observed previously in implanted and pulsed laser melted GaAs [30,46]. Additionally, after the PLM process, an interface surface-layer of oxide with thickness around 5–10 nm appears for all the samples.

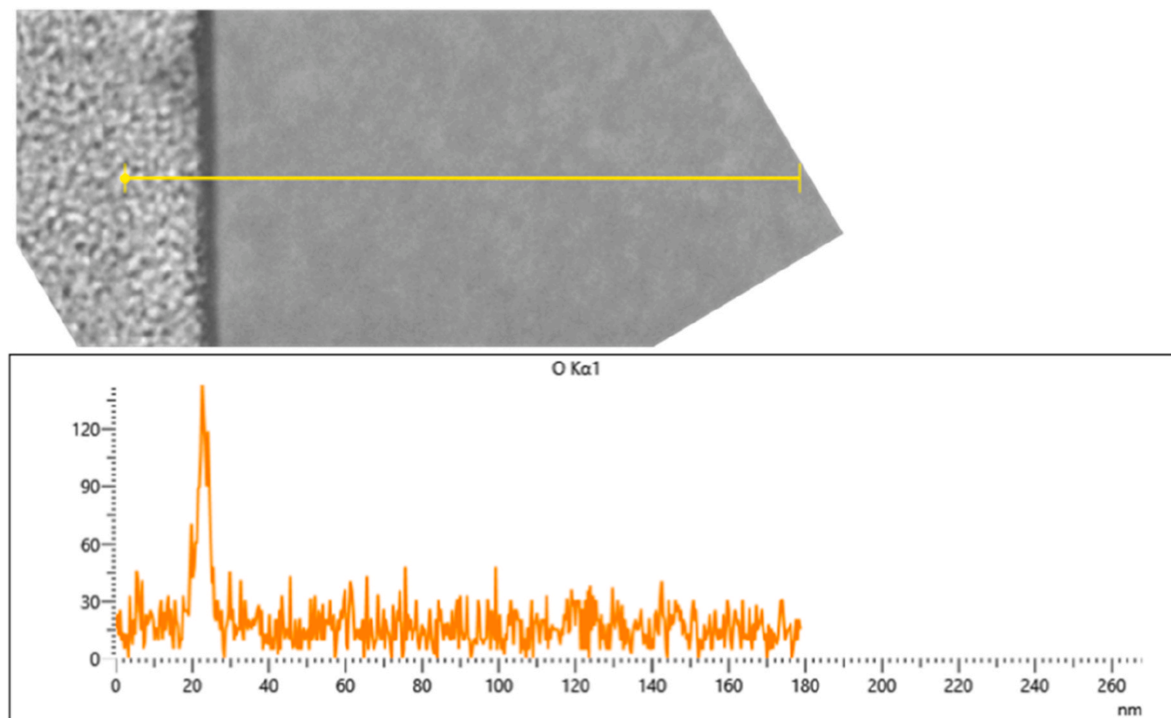

Fig. 8. EDS signal of GaAs processed by PLM at 0.50 J/cm^2 laser fluence. Top: Measurement path. Bottom: O signal.

Fig. 6 show the STEM images of samples laser melted with (0.40, 0.50 and 0.65 J/cm^2). The STEM images show the bubble-like structures more clearly. The bubble-like structures are more clearly observed in the STEM images as a darker spot, distributed over the implanted region and in some cases at the surface.

Since the bubbles only appear for the implanted samples, they may be related to the presence of Ti. This have been analysed using EDS spectroscopy. The minimum detectable concentration with our equipment is 1% atomic percentage. Therefore, it is not possible to obtain an accurate profile of the Ti concentration, but it is possible to detect regions with higher Ti concentrations. Fig. 7 shows the EDS signal for Ti and O obtained along a path from the surface to the implanted layer, for the implanted sample processed at 0.50 J/cm^2. Ti is detected at the surface and within the bubble-like structure appearing at approximately 60 nm from the surface. Furthermore, EDS maps were created to assess the distribution of Ti within the implanted layer. The map shows that an oxide layer is present on the surface of the sample and Ti is distributed on the surface of the samples and within the implanted layer, and not only present in the bubble-like structures, which agrees with ToF-SIMS results. (Check Fig. 4.1 in supplementary document).

This indicate that these structures are indeed related to an accumulation of Ti. For this measurement, a bubble structure is also observed at the surface. This can relate to the high concentration of Ti observed in SIMS measurement on the first 10 nm of the sample. O signal is also observed at the surface for all the PLM processed samples, indicating an appearance of a surface oxide layer. Fig. 8 shows the EDS signal for a non-implanted PLM processed sample at the same PLM energy fluence (0.50 J/cm^2). As expected, no Ti signal was detected, but the O signal at the surface does appear. Therefore, we conclude that the oxide surface layer is related to the PLM process itself and not specifically to the presence of Ti. A similar result was observed for GaP processed at the same conditions and the resulting layer proved to act as a passivation layer, adding value to the PLM process [16]. Since this work is focused on the recrystallization of the implanted layer, we have not conducted further analysis (such as XPS) of the surface oxide layer.

In a future paper, the electrical and photo-response properties of the supersaturated layers will be analysed in detail. Hall effect measurements have been performed to obtain the mobility of the samples. While a decrease of the mobility with respect to the reference substrate (Hall mobility of 4092 cm^{2}V^{-1}s^{-1}) is obtained for the implanted samples, high mobility values have been measured (in the 1500–2100 cm^{2}V^{-1}s^{-1} range, depending on the PLM energy), further supporting the crystalline recovery demonstrated by the structural characterisation presented in this work. For just PLM processed samples, mobilities as high as 4078 cm^{2}V^{-1}s^{-1} (no real difference with respect to the substrate) have been measured for a 0,65 J/cm^{-2} PLM fluence.

Concerning Ga and As vacancies EDS results show no detectable changes on the signal of Ga and As after recrystallization using PLM. However, there is a detectable change on the signal of Ga and As at the location where the bubble-like structure appear (Check supplementary document Fig. 5.1). This can be explained by Ti accumulating at the bubble-like structure.

4. Conclusion

In this work, semi-insulating GaAs was implanted with Ti with a dose of 2×10^{15} cm^{-2} and subsequently processed by pulsed laser melting, at different fluences in the 0.30 J/cm^2 – 0.65 J/cm^2 range. Incorporation of Ti above the theoretical Mott limit has been shown by ToF-SIMS results with the recovery of the crystallinity for PLM fluences of up to 0.65 J/cm^2 as demonstrated by Raman spectroscopy, TEM, and STEM results. EDS results show surface oxide layer. Bubble-like structures in which the Ti concentration is higher are also observed. The suitability of ion implantation followed by PLM to obtain crystalline GaAs supersaturated with Ti concentrations above the insulator to metal transition has been demonstrated.

CRediT authorship contribution statement

S. Algaidy: Visualization, Validation, Software, Resources, Project administration, Methodology, Investigation, Formal analysis, Data curation, Conceptualization, Writing – original draft, Writing – review & editing. **D. Caudevilla:** Writing – review & editing. **F. Perez-Zenteno:** Writing – review & editing. **R. García-Hernansanz:** Writing – review &

editing. **E. García-Hemme:** Writing – review & editing. **J. Olea:** Writing – review & editing, Funding acquisition, Conceptualization. **E. San Andrés:** Writing – review & editing, Project administration, Funding acquisition. **S. Duarte-Cano:** Writing – review & editing. **J. Siegel:** Writing – review & editing, Investigation. **J. Gonzalo:** Writing – review & editing, Investigation. **D. Pastor:** Writing – review & editing, Visualization, Validation, Supervision, Resources, Project administration, Methodology, Investigation, Funding acquisition, Formal analysis, Conceptualization. **A. del Prado:** Writing – review & editing, Visualization, Validation, Supervision, Resources, Project administration, Methodology, Funding acquisition, Formal analysis, Conceptualization.

Declaration of competing interest

The authors declare the following financial interests/personal relationships which may be considered as potential competing interests: Sari Algaidy reports financial support was provided by Kingdom of Saudi Arabia Ministry of Education. Daniel Caudevilla reports financial support was provided by European Social Fund. Francisco Perez-Zentero reports financial support was provided by Mexico CONACyT. Sari Algaidy reports financial support was provided by Comunidad Autonoma de Madrid. Sari Algaidy reports financial support was provided by Ministerio de Economía y Competitividad. Sari Algaidy reports financial support was provided by Ministerio de Economía y Competitividad.

Data availability

Data will be made available on request.

Acknowledgement

Authors would like to acknowledge C.A.I. de Técnicas Físicas of the Universidad Complutense de Madrid for ion implantation, and the technical. This work was partially supported by the Project MADRID-PV2 (Grant No. P20138/EMT-4308) funded by the Comunidad Autónoma de Madrid with the support of FEDER funds, by the Spanish MINECO (Ministerio de Economía y Competitividad) under grants PID2020-116508RB-I00, PID2020-117498RB-I00 and RTI2018-096498-B-I00. One of the authors (S. Algaidy) would also like to acknowledge financial support from Ministry of Education in the Kingdom of Saudi Arabia. D.Caudevilla would also like to acknowledge a grant (PRE2018-083798), financed by MICINN and European Social Fund. F. Perez-Zenteno would like to acknowledge financial support Mexico grant program CONACyT under grant 786327. The authors would like to also acknowledge the services of CAI de Espectroscopia of UCM, (INA-LMA) de Universidad de Zaragoza and C.A.C.T.I de Universidad de Vigo for Raman, FIB-SEM and SIMS, respectively.

Appendix A. Supplementary data

Supplementary data to this article can be found online at https://doi.org/10.1016/j.mssp.2022.107191.

References

[1] A. Luque, A. Martí, Increasing the efficiency of ideal solar cells by photon induced transitions at intermediate levels, Phys. Rev. Lett. 78 (26) (1997) 5014.
[2] P. Palacios, P. Wahnón, S. Pizzinato, J.C. Conesa, Energetics of formation of Ti Ga 3 As 4 and Ti Ga 3 P 4 intermediate band materials, J. Chem. Phys. 124 (1) (2006), 014711.
[3] A. Luque, A. Martí, E. Antolín, C. Tablero, Intermediate bands versus levels in non-radiative recombination, Phys. B Condens. Matter 382 (1-2) (2006) 320–327.
[4] W. Wang, A.S. Lin, J.D. Phillips, Intermediate-band photovoltaic solar cell based on ZnTe: O, Appl. Phys. Lett. 95 (1) (2009), 011103.
[5] K.M. Yu, W. Walukiewicz, J. Wu, W. Shan, J.W. Beeman, M.A. Scarpulla, O. D. Dubon, P. Becla, Diluted II-VI oxide semiconductors with multiple band gaps, Phys. Rev. Lett. 91 (24) (2003), 246403.
[6] A. Luque, A. Marti, The intermediate band solar cell: progress toward the realization of an attractive concept, Adv. Mater. 22 (2) (2010) 160–174.
[7] P. Palacios, K. Sánchez, J.C. Conesa, J.J. Fernández, P. Wahnón, Theoretical modelling of intermediate band solar cell materials based on metal-doped chalcopyrite compounds, Thin Solid Films 515 (15) (2007) 6280–6284.
[8] P.D. Persans, N.E. Berry, D. Recht, D. Hutchinson, H. Peterson, J. Clark, S. Charnvanichborikarn, J.S. Williams, A. DiFranzo, M.J. Aziz, J.M. Warrender, Photocarrier lifetime and transport in silicon supersaturated with sulfur, Appl. Phys. Lett. 101 (11) (2012), 111105.
[9] J.P. Mailoa, A.J. Akey, C.B. Simmons, D. Hutchinson, J. Mathews, J.T. Sullivan, D. Recht, M.T. Winkler, J.S. Williams, J.M. Warrender, P.D. Persans, Room-temperature sub-band gap optoelectronic response of hyperdoped silicon, Nat. Commun. 5 (1) (2014) 1–8.
[10] E. García-Hemme, D. Caudevilla, S. Algaidy, F. Pérez-Zenteno, R. García-Hernansanz, J. Olea, D. Pastor, Á. del Prado, E. San Andrés, I. Mártil, G. González-Díaz, On the optoelectronic mechanisms ruling Ti-hyperdoped Si photodiodes, Advanced Electronic Materials 8 (2) (2022), 2100788.
[11] E. Garcia-Hemme, G. García, P. Palacios, D. Montero, R. García-Hernansanz, G. Gonzalez-Diaz, P. Wahnon, Vanadium supersaturated silicon system: a theoretical and experimental approach, J. Phys. Appl. Phys. 50 (49) (2017), 495101.
[12] M. Wang, E. García-Hemme, Y. Berencén, R. Hübner, Y. Xie, L. Rebohle, C. Xu, H. Schneider, M. Helm, S. Zhou, Silicon-based intermediate-band infrared photodetector realized by Te hyperdoping, Adv. Opt. Mater. 9 (4) (2021), 2001546.
[13] Y. Berencén, S. Prucnal, F. Liu, I. Skorupa, R. Hübner, L. Rebohle, S. Zhou, H. Schneider, M. Helm, W. Skorupa, Room-temperature short-wavelength infrared Si photodetector, Sci. Rep. 7 (1) (2017) 1–9.
[14] S. Silvestre, A. Boronat, M. Colina, L. Castañer, J. Olea, D. Pastor, A. del Prado, I. Mártil, G. González Díaz, A. Luque, E. Antolín, E. Hernández, I. Ramiro, I. Artacho, E. López, A. Martí, Sub-bandgap external quantum efficiency in Ti implanted Si heterojunction with intrinsic thin layer cells, Jpn. J. Appl. Phys. 52 (2013), 122302.
[15] H.H. Gandhi, D. Pastor, T.T. Tran, S. Kalchmair, L.A. Smilie, J.P. Mailoa, R. Milazzo, E. Napolitani, M. Loncar, J.S. Williams, M.J. Aziz, Gold-hyperdoped Germanium with room-temperature sub-band-gap optoelectronic response, Physical Review Applied 14 (6) (2020), 064051.
[16] J. Olea, A. del Prado, E. García-Hemme, R. García-Hernansanz, D. Montero, G. González-Díaz, J. Gonzalo, J. Siegel, E. López, Strong subbandgap photoconductivity in GaP implanted with Ti, Prog. Photovoltaics Res. Appl. 26 (3) (2018) 214–222.
[17] J. Olea, D. Pastor, M. Toledano-Luque, I. Mártil, G. González-Díaz, J. Ibáñez, R. Cuscó, Y.L. Artús, Ti-doped gallium phosphide layers with concentrations above the Mott limit, MRS Online Proc. Libr. 1210 (1) (2009) 1–6.
[18] D. Pastor, J. Olea, M. Toledano-Luque, I. Mártil, G. González-Díaz, J. Ibáñez, R. Cuscó, L. Artús, Laser thermal annealing effects on single crystal gallium phosphide, J. Appl. Phys. 106 (5) (2009), 053510.
[19] N. López, L.A. Reichertz, K.M. Yu, K. Campman, W. Walukiewicz, Engineering the electronic band structure for multiband solar cells, Phys. Rev. Lett. 106 (2) (2011), 028701.
[20] J.S. Blakemore, Semiconducting and other major properties of gallium arsenide, J. Appl. Phys. 53 (10) (1982) R123–R181.
[21] I. Ramiro, A. Martí, Intermediate band solar cells: present and future, Prog. Photovoltaics Res. Appl. 29 (7) (2021) 705–713.
[22] S. Golovynskyi, O.I. Datsenko, L. Seravalli, G. Trevisi, P. Frigeri, E. Gombia, I. S. Babichuk, D. Lin, B. Li, J. Qu, Near-infrared lateral photoresponse in InGaAs/GaAs quantum dots, Semicond. Sci. Technol. 35 (5) (2020), 055029.
[23] X. Zhu, F. Lin, Z. Zhang, X. Chen, H. Huang, D. Wang, J. Tang, X. Fang, D. Fang, J. C. Ho, L. Liao, Enhancing performance of a GaAs/AlGaAs/GaAs nanowire photodetector based on the two-dimensional electron–hole tube structure, Nano Lett. 20 (4) (2020) 2654–2659.
[24] H. Tian, A. Hu, Q. Liu, X. He, X. Guo, Interface-induced high responsivity in hybrid graphene/GaAs photodetector, Adv. Opt. Mater. 8 (8) (2020), 1901741.
[25] Z. Tao, D. Zhou, H. Yin, B. Cai, T. Huo, J. Ma, Z. Di, N. Hu, Z. Yang, Y. Su, Graphene/GaAs heterojunction for highly sensitive, self-powered Visible/NIR photodetectors, Mater. Sci. Semicond. Process. 111 (2020), 104989.
[26] S.M. Fike, B. Buchanan, N.M. Jokerst, M.A. Brooke, T.G. Morris, S.P. DeWeerth, 8 x 8 array of thin-film photodetectors vertically electrically interconnected to silicon circuitry, IEEE Photon. Technol. Lett. 7 (10) (1995) 1168–1170.
[27] A.V. Kudrin, V.P. Lesnikov, Y.A. Danilov, M.V. Dorokhin, O.V. Vikhrova, P. B. Demina, D.A. Pavlov, Y.V. Usov, V.E. Milin, Y.M. Kuznetsov, R.N. Kriukov, High-temperature intrinsic ferromagnetism in heavily Fe-doped GaAs layers, Semicond. Sci. Technol. 35 (12) (2020), 125032.
[28] S. Kumar, G.B. Corrêa Jr., C. Devi, D. Jacobsson, A. Johannes, C. Ronning, W. Paraguassu, W. Paschoal Jr., H. Pettersson, Evaluation of carrier density and mobility in Mn ion-implanted GaAs: Zn nanowires by Raman spectroscopy, Nanotechnology 31 (20) (2020), 205705.
[29] H. Ullrich, A. Knecht, D. Bimberg, H. Kräutle, W. Schlaak, Defect-induced redistribution of Fe-or Ti-implanted and annealed GaAs, InAs, GaP, and InP, J. Appl. Phys. 72 (8) (1992) 3514–3521.
[30] T. Kim, M.R. Pillai, M.J. Aziz, M.A. Scarpulla, O.D. Dubon, K.M. Yu, J.W. Beeman, M.C. Ridgway, Heat flow model for pulsed laser melting and rapid solidification of ion implanted GaAs, J. Appl. Phys. 108 (1) (2010), 013508.
[31] H. Abe, H. Harima, S.I. Nakashima, M. Tani, K. Sakai, Y. Tokuda, K. Kanamoto, Y. Abe, Characterization of crystallinity in low-temperature-grown GaAs layers by Raman scattering and time-resolved photoreflectance measurements, Jpn. J. Appl. Phys. 35 (12R) (1996) 5955.

[32] R. Huang, T. Lan, C. Li, J. Li, Z. Wang, The structural evolution of light-ion implanted into GaAs single crystal after annealing, Nucl. Instrum. Methods Phys. Res. Sect. A Accel. Spectrom. Detect. Assoc. Equip. 1005 (2021), 165395.
[33] S.U. Campisano, G. Foti, E. Rimini, F.H. Eisen, W.F. Tseng, M.A. Nicolet, J. L. Tandon, Laser pulse annealing of ion-implanted GaAs, J. Appl. Phys. 51 (1) (1980) 295–298.
[34] J. Solis, C.N. Afonso, J. Piqueras, Excimer laser melting of GaAs: real-time optical study, J. Appl. Phys. 71 (2) (1992) 1032–1034.
[35] J.F. Ziegler, M.D. Ziegler, J.P. Biersack, SRIM–The stopping and range of ions in matter (2010), Nucl. Instrum. Methods Phys. Res. Sect. B Beam Interact. Mater. Atoms 268 (11-12) (2010) 1818–1823.
[36] M.A. Shahid, B.J. Sealy, K.E. Puttick, The laser energy window for ion-implanted GaAs, J. Mater. Sci. 19 (12) (1984) 3887–3894.
[37] W. Wesch, G. Götz, Rapid annealing of ion-implanted GaAs, Phys. Status Solidi 94 (2) (1986) 745–766.
[38] F. Liu, S. Prucnal, R. Hübner, Y. Yuan, W. Skorupa, M. Helm, S. Zhou, Suppressing the cellular breakdown in silicon supersaturated with titanium, J. Phys. Appl. Phys. 49 (24) (2016), 245104.
[39] J. Narayan, C.W. White, O.W. Holland, M.J. Aziz, Phase transformation and impurity redistribution during pulsed laser irradiation of amorphous silicon layers, J. Appl. Phys. 56 (6) (1984) 1821–1830.
[40] M.O. Thompson, G.J. Galvin, J.W. Mayer, P.S. Peercy, J.M. Poate, D.C. Jacobson, A.G. Cullis, N.G. Chew, Melting temperature and explosive crystallization of amorphous silicon during pulsed laser irradiation, Phys. Rev. Lett. 52 (26) (1984) 2360.
[41] H. Birey, J. Sites, Radiative transitions induced in gallium arsenide by modest heat treatment, J. Appl. Phys. 51 (1) (1980) 619–624.
[42] R. Ashokan, K.P. Jain, H.S. Mavi, M. Balkanski, Raman study of phosphorous-implanted and pulsed laser-annealed GaAs, J. Appl. Phys. 60 (6) (1986) 1985–1993.
[43] J. Wagner, Raman spectroscopy for impurity characterization in III–V semiconductors, Appl. Surf. Sci. 50 (1-4) (1991) 79–86.
[44] S. Mishra, D. Kabiraj, A. Roy, S. Ghosh, Effect of high-energy light-ion irradiation on SI-GaAs and GaAs: Cr as observed by Raman spectroscopy, J. Raman Spectrosc. 43 (2) (2012) 344–350.
[45] J. Wang, H. Mao, Z. Zhu, Q. Zhao, Z. Li, W. Lu, Recrystallization behavior of high-fluence N+-implanted GaAs studied by Raman spectroscopy, Appl. Surf. Sci. 252 (6) (2006) 2186–2190.
[46] K.M. Yu, W. Walukiewicz, M.A. Scarpulla, O.D. Dubon, J. Wu, J. Jasinski, Z. Liliental-Weber, J.W. Beeman, M.R. Pillai, M.J. Aziz, Synthesis of GaN x As 1− x thin films by pulsed laser melting and rapid thermal annealing of N+-implanted GaAs, J. Appl. Phys. 94 (2) (2003) 1043–1049.